# Laser Melting of Alumina-Coated Steel

**S. Z. Shuja and B. S. Yilbas**
Dept. of Mechanical Engineering, KFUPM, Dhahran 31261, Saudi Arabia

*DOI 10.1002/aic.12467*
*Published online November 29, 2010 in Wiley Online Library (wileyonlinelibrary.com).*

*Laser melting of alumina-coated steel surface is considered. Temperature field and phase change in the alumina coating and steel are predicted numerically using the control volume approach. The repetitive laser pulses with 60% duty cycle are incorporated in the analysis. The porosity-enthalpy method is adapted to account for the phase change. It is found that steel at alumina coating interface undergoes a melting before alumina after the end of heating of the 2nd pulse. The melt pool size of alumina is smaller than that corresponding to steel. The resolidification of the melt pool takes place in the alumina coating, whereas the melt pool remains in steel beneath the alumina coating during the cooling cycle.* © 2010 American Institute of Chemical Engineers *AIChE J,* 57: 2547–2554, 2011
*Keywords: laser, heating, melting, alumina, steel*

## Introduction

Laser control melting of ceramic coatings provides thermal integration between the coating and the base substrate. The control melting results in homogeneous microstructures at the surface and improves the bonding of the coating to the base material. Moreover, the differences in the thermal properties of the coating and the base material, and the small-coating thickness result in differences in the size of the melting zones in the coating and in the substrate material. Laser remelting of surfaces is involved with the Marangoni flow in the melt pool. This is because of the surface tension force gradient acting at the free surface of the melt pool. However, the model studies provide useful information on the melting process and the effecting parameters. In addition, it reduces the experimental cost and the time. Consequently, modeling of the laser melting of two-layer assembly, consisting of thin layer ($\approx$10 $\mu$m) at the top and the base material at the bottom, including the Marangoni effect becomes essential.

Considerable research is carried out to examine the laser heating of solids and phase change in the laser irradiated region. The phase change during the laser drilling process was studied by Zhang and Faghri.[1] They indicated that the heat conduction between the melt pool and solid substrate beneath the surface influenced the liquid layer thickness significantly. The melt pool characteristics during the laser processing of steel surface were investigated by Yang et al.[2] They indicated that the Marangoni flow in the melt pool altered the melt pool size and influenced the cooling rates for solidification. Chakraborty and Dutta[3] studied heat and mass transfer during the laser surface alloying of a solid. They used a numerical model in corporating the nonequilibrium solidification in the melt pool. The melt geometry in relation to laser cutting process was examined by Tani et al.[4] They indicated that two mechanisms governed the dross attachment due to molten flow at the kerf surface. The first was linked to the injection speed of the liquid phase from the kerf bottom and the second mechanism was associated with the occlusion of the kerf bottom through an excess of molten metal, which resulted in incomplete injection of molten material. Laser induced melting and solidification of metals were investigated by Chung and Das.[5] They developed relations between the duration for initiation of the melting and the laser melting parameters. The laser melting of ceramics was studied Li et al.[6] They predicted the melt depth and melt size in the irradiated region, which agreed well with the experimental data. The material removal mechanisms in pulsed laser fusion cutting of ceramics were examined by Quintero et al.[7] They showed that the molten mass flow promoted by the momentum transfer from the assisting gas jet was predominated at high-laser frequencies, whereas the material ejected due to recoil pressure was the main

Correspondence concerning this article should be addressed to B. S. Yilbas at bsyilbas@kfupm.edu.sa.

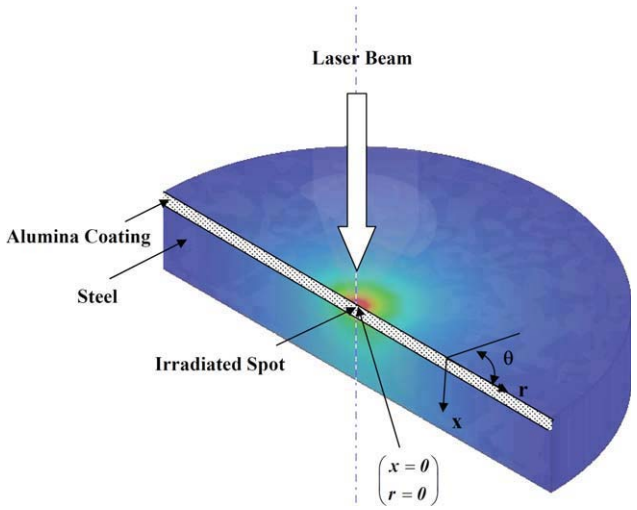


**Figure 1. A schematic view of the laser heating of alumina coated steel.**

[Color figure can be viewed in the online issue, which is available at wileyonlinelibrary.com.]

molten mass flow at the low-laser frequencies. The influence of laser beam geometry on the transformation hardening of steel surface was investigated by Safdar et al.[8] They showed that the beam geometry had significant effect on the hardening of the surface; in which case, triangular beam geometry produced improved transformation and highest hardness values at the surface because of slower heating without sacrificing the processing rate and hardening depths. The resolidification of a subcooled metal powder particle subjected to nanosecond laser heating was examined by Konrad et al.[9] They showed that the laser flounce and particle diameter were the most affecting parameters on the melting and solidification times. The solid-liquid phase change due to the pulsed heating was investigated by Krishnan et al.[10] They indicated that the decrease in Stefan number reduced the rate of melting due to the thermal inertia associated with the phase change and the relative increase in the latent heat of fusion. Laser induced melting in the irradiated surface of steel was investigated by Yilbas et al.[11–13] and Bin-Mansoor et al.[14,15] They showed that the phase change could be modeled using the energy method in the irradiated region. Shuja et al.[16,17] investigated the surface melting of steel and influence of the Marangoni flow on temperature distribution in the melt pool.

The previous investigations[11–17] were limited to the single layer heating situation. In some practical applications, such as hard coatings, laser treatment of two-layered structures becomes fruitful. In this study, laser melting of ceramic coatings deposited on to the steel surface is investigated. The numerical scheme using the control volume approach is introduced to solve the governing equations of flow and heat transfer. The porosity-enthalpy method is incorporated to

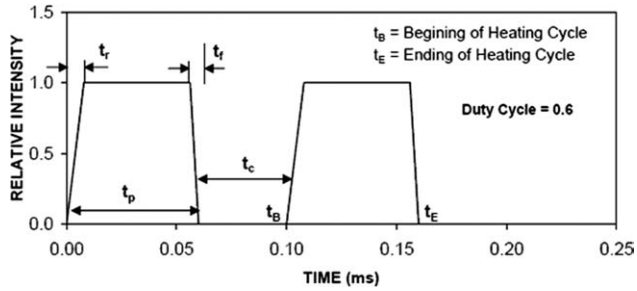


**Figure 2. Temporal distribution of laser repetitive two pulses.**

account for the phase change process. An experiment is carried out to compare the melt depth predicted and obtained from the experiment.

## Mathematical Analysis of Heating

The laser heating situation is shown in Figure 1. The heat-transfer equation in relation to the laser heating process can be written as:

$$\rho \frac{DE}{Dt} = (\nabla(k\nabla T)) + S_o \tag{1}$$

where $E$ is the energy gain by the substrate material, $k$ is the thermal conductivity, $\rho$ is the density, and $S_o$ is the volumetric heat source term and it is:

$$S_o = I_o \delta(1 - r_f) \exp(-\delta_Z) \exp\left(-\left(\frac{r}{a} - \beta\right)^2\right) f(t) \tag{2}$$

$I_o$ is laser peak intensity, $\delta$ is the absorption depth, $r_f$ is the surface reflectivity, $f(t)$ is the temporal distribution of the laser repetitive pulses (Figure 2), $a$ is the Gaussian parameter, and $\beta$ is the laser intensity parameter. The temporal variation of laser pulse intensity is considered to be in trapezium shape in time domain. The temporal variation of the laser pulse shape, which is trapezium in time domain, resembles almost the actual laser pulse shape used in the industry. The laser pulse parameters used in the simulations are given in Table 1. The time function ($f(t)$, Figure 2) representing the consecutive pulses is:

$$f(t) = \begin{Bmatrix} 0, & t = 0 \\ 1, & t_r \le t \le t_f \\ 0, & t = t_p \\ 0, & t_p \le t \le t_c \end{Bmatrix}$$

where $t_r$ is the pulse rise time, $t_f$ is the pulse fall time, $t_p$ is the pulse length, $t_c$ is the end of cooling period. $f(t)$ repeats when the second consecutive pulse begins, provided that time $t = t_f + t_c$ corresponds to the starting time of the second pulse. The same mathematical arguments can apply for the other consecutive pulses after the second pulse.

Because the heated substrate material is stationary, the convective terms drop and Eq. 1 reduces to:

**Table 1. Laser Pulse Parameters Used in the Simulations**

| | Laser Pulse Length, $t_p$ (ms) | Cooling Period, $t_c$ (ms) | Pulse Rise Time, $t_r$ (ms) | Pulse Fall Time, $t_f$ (ms) | Pulse Intensity (W/m$^2$) $\times 10^{10}$ | Guassian Parameter, $a$ (m) |
|---|---|---|---|---|---|---|
| Duty Cycle 60% | 0.06 | 0.04 | 0.0078 | 0.0039 | 0.6 | $3 \times 10^{-4}$ |

$$\rho\frac{\partial(C_pT)}{\partial t}=(\nabla(k\nabla T))+S_o \tag{3}$$

In the case of solid heating, two boundary conditions for each principal axis are specified. Because of the low-absorption depth, at a distance considerably away from the surface (at infinity) it is assumed that the heating has no effect on the temperature of the slab; consequently, at a depth of infinity, the temperature is assumed to be constant and equal to the initial temperature of the slab. However, at alumina-steel interface the continuity of flux and temperature is incorporated. The boundary conditions, therefore, are:

$$z \text{ at infinity} \Rightarrow \quad z=\infty : T(r,\infty,t)=T_o \text{ (specified)}$$
$$r \text{ at infinity} \Rightarrow \quad r=\infty : T(\infty,z,t)=T_o \text{ (specified)}$$
$$\text{At symmetry axis} \Rightarrow \quad r=0 : \frac{\partial T(0,z,t)}{\partial r}=0$$
$$\text{At the surface} \Rightarrow \; z=0 : k\frac{\partial T}{\partial z}=h_t(T_s-T_\infty)+\sigma(T_s^4-T_\infty^4)$$

where $h_t$ is the heat-transfer coefficient at the free surface and $\sigma$ is the Stefan-Boltzmann constant. The heat-transfer coefficient predicted earlier is used in the present simulations [$h_t = 10^4$ W/(m$^2$ K)].[18]

At the alumina-steel interface:

$$z=z_t : k_a\frac{\partial T}{\partial z}=k_s\frac{\partial T}{\partial z}$$

where $k_a$ and $k_s$ are the thermal conductivity of alumina and steel, respectively, and $z_t$ is the alumina coating thickness (10 $\mu$m).

The laser beam axis is the $z$-axis (Figure 1). Equation 3 is solved numerically with the appropriate boundary conditions to predict the temperature field in the substrate material. However, to analyze the phase change problem, the enthalpy-porosity technique is used. In this case, the melt interface is tracked explicitly after defining a quantity called the liquid fraction, which indicates the fraction of the cell volume that is in liquid form. Based on the enthalpy balance, the liquid fraction is computed. The mushy zone is a region in which the liquid fraction lies between 0 and 1. The mushy zone is modeled as a "pseudo" porous medium in which the porosity decreases from 1 to 0 as the material solidifies. When the material has fully solidified in a cell, the porosity becomes zero and hence the velocities also drop to zero.[19,20]

The enthalpy of the material is computed as the sum of the sensible enthalpy, $h$, and the latent heat, $\Delta H$:

$$H=h+\Delta H \tag{4}$$

where

$$h=h_{ref}+\int_{T_{ref}}^{T}c_p dT \tag{5}$$

and $h_{ref}$ is reference enthalpy, $T_{ref}$ is reference temperature, and $\boldsymbol{c}_p$ is specific heat at constant pressure.

The liquid fraction, $\beta_l$, can be defined as:

$$\beta_l=0 \text{ if } T<T_{solidus}$$
$$\beta_l=1 \text{ if } T>T_{liquidus}$$
$$\beta_l=\frac{T-T_{solidus}}{T_{liquidus}-T_{solidus}} \text{ if } T_{solidus}<T<T_{liquidus} \tag{6}$$

Equation 6 is referred to as the lever rule.[19,20]

The latent heat content can now be written in terms of the latent heat of the material, $L$:

$$\Delta H=\beta_l L \tag{7}$$

The latent heat content can vary between zero (for a solid) and $L$ (for a liquid).

The enthalpy-porosity technique treats the mushy region (partially solidified region) as a porous medium. The porosity in each cell is set equal to the liquid fraction in that cell. In fully solidified regions, the porosity is equal to zero, which extinguishes the velocities in these regions. The flow in the mushy zone is governed by the Darcy law. In this case, as the porosity in the mushy zone decreases, the permeability and the velocity also decrease, i.e., when the mushy zone becomes completely solid at the interface of the mushy zone-solid phase, velocity reduces to zero. This behavior can be accounted for by defining the momentum sink as $S_z=-A(\bar{v})$, where $A$ is obtained from Carman-Koseny equation[20]; in which case, it is shown that $A=\frac{(1-\beta_l)^2}{(\beta_l^3+\varepsilon)}A_{mush}$.[20] Therefore, the momentum sink due to the reduced porosity in the mushy zone takes the following form[19,20]:

$$S_z=\frac{(1-\beta_l)^2}{(\beta_l^3+\varepsilon)}A_{mush}(\vec{v}) \tag{8}$$

where $\beta_l$ is the liquid volume fraction, $\varepsilon$ is a small number (0.001) to prevent division by zero, $A_{mush}$ is the mushy zone constant. The mushy zone constant measures the amplitude of the damping; the higher this value, the steeper the transition of the velocity of the material to zero as it solidifies. The liquid velocity can be found from the average velocity is determined from:

$$\vec{v}_{liq}=\frac{\vec{v}}{\beta_l} \tag{9}$$

The solution for temperature is essentially iteration between the energy equation (Eq. 3) and the liquid fraction equation (Eq. 6). Directly using Eq. 4 to update the liquid fraction usually results in poor convergence of the energy equation. However, the method suggested by Voller and Prakash[19] is used to update the liquid fraction based on the specific heat.

The continuity and momentum equations in the melt layer are different than that corresponding to the mushy zone. Therefore, the conservation equations need to be incorporated to account for the flow field. This problem is governed by the axisymmetric Navier-Stokes equation. For laminar flow, the conservation equations are:

$$\text{Continuity} \quad \frac{\partial u}{\partial x}+\frac{1}{r}\frac{\partial(rv)}{\partial r}=0$$
$$r-\text{dir} \quad \frac{\partial v}{\partial t}+u\frac{\partial v}{\partial x}+v\frac{\partial v}{\partial r}=-\frac{1}{\rho}\frac{\partial p}{\partial r}+\frac{\mu}{\rho}\left(\frac{\partial^2 v}{\partial x^2}+\frac{1}{r}\frac{\partial}{\partial r}\left(r\frac{\partial v}{\partial r}\right)-\frac{v}{r^2}\right)$$
$$x-\text{dir} \quad \frac{\partial u}{\partial t}+u\frac{\partial u}{\partial x}+v\frac{\partial u}{\partial r}=-\frac{1}{\rho}\frac{\partial p}{\partial x}+\frac{\mu}{\rho}\left(\frac{\partial^2 u}{\partial x^2}+\frac{1}{r}\frac{\partial}{\partial r}\left(r\frac{\partial u}{\partial r}\right)\right)+g\beta_E T+S_z$$
$$\text{Energy} \quad \rho\frac{\partial(\rho H)}{\partial t}+\nabla\cdot(\rho\,\bar{v}H)=\nabla\cdot(k\nabla T)+S_o-S_h$$

or

$$\frac{\partial T}{\partial t}+u\frac{\partial T}{\partial x}+v\frac{\partial T}{\partial r}=\alpha\left(\frac{\partial^2 T}{\partial x^2}+\frac{1}{r}\frac{\partial}{\partial r}\left(r\frac{\partial T}{\partial r}\right)\right)+S_o-S_h \tag{10}$$

Table 2. Material Properties Used in the Simulations[22]

| | Temp. (K) | 300 | 400 | 600 | 800 | 1000 | 1200 | 1500 |
|---|---|---|---|---|---|---|---|---|
| Steel | $C_p$ [J/(kg K)] | 477 | 515 | 557 | 582 | 611 | 640 | 682 |
| | $K$ [W/(m K)] | 14.9 | 16.6 | 19.8 | 22.6 | 25.4 | 28 | 31.7 |
| | $\rho$ (kg/m$^3$) | 8018 | 7968 | 7868 | 7769 | 7668 | 7568 | 7418 |
| Alumina | $C_p$ [J/(kg K)] | 786.19 | 939.53 | 1019.86 | 1140.27 | 1190.84 | 1234.22 | 1254.52 |
| | $K$ [W/(m K)] | 37.06 | 28.19 | 21.81 | 11.56 | 8.63 | 7.12 | 6.66 |
| | $\rho$ (kg/m$^3$) | 3800 | – | – | – | – | – | – |

The solidus and liquidus temperatures of steel are 1766 K and 1788 K, whereas solidus and liquidus temperatures of alumina are 2260 K and 2323 K, respectively. The latent heat of melting for steel is 400,000 J/kg and for alumina is 900,000 J/kg.

where $u$ and $v$ are the component of the velocity in the radial $r$ and axial $x$ directions, respectively, $p$ is the pressure, $T$ is the temperature, $\alpha$ is the thermal diffusivity of the molten material, $\beta_E$ is the volumetric thermal expansion coefficient, which is formulated using the Boussinesq approximation, $S_z$ is the momentum sink due to the reduced porosity in the mushy zone (Eq. 8), and $S_h$ is a phase related source term convection-diffusion phase change ($S_h = \rho \frac{\partial(\rho \Delta H)}{\partial t} + \nabla.(\rho \bar{v} \Delta H)$, where $\Delta H = H - \rho C_p T$).[20] The term $g\beta_E T$ is the buoyancy term, which is used to introduce natural convection in the melt pool. The energy equation is similar to Eq. 3, provided that Eq. 10 is the enthalpy equation and being used for the phase change and the liquid phase during the laser heating process. Moreover, a zero reference temperature has been assumed for the buoyancy force term in the $z$-direction momentum equation. Boundary conditions for Eq. 10 are as follows:

Free surface (at $x = 0$)

$$\mu \frac{\partial v}{\partial x} = -\sigma_T \frac{\partial T}{\partial r}$$
$$u = 0$$
$$-k \frac{\partial T}{\partial x} = q_{loss}$$

where $q_{loss}$ includes the convective losses from the surface. The heat transfer coefficient is taken as $h_t = 10^4$ W/(m$^2$ K) at the surface.[18]

Axis of symmetry (at $r = 0$)

$$v = 0$$
$$\frac{\partial u}{\partial r} = 0$$
$$\frac{\partial T}{\partial r} = 0$$

Far field (solid)

$$T = T_0$$

where $T_o$ is the ambient temperature. The equation $\mu \frac{\partial v}{\partial x} = -\sigma_T \frac{\partial T}{\partial r}$ states the balance between the surface tension force and the viscous force on the free surface, where $\sigma_T$ is the temperature coefficient of surface tension, which is a property of the material.

## Numerical Solution

To discretize the governing equations, a control volume approach is introduced. The details of the numerical scheme are given in Ref. 21. The calculation domain is divided into grids and a grid independence test is performed for different grid sizes and orientation. A nonuniform grid with 90 × 55 mesh points along $x$- and $r$-axes, respectively, is used after securing the grid independence. The finer grids are located near the irradiated spot center in the vicinity of the surface and grids become courser as the distance increases toward the bulk of substrate material. The central difference scheme is adopted for the diffusion terms. The convergence criterion for the residuals is set as $\left|\psi^k - \psi^{k-1}\right| \leq 10^{-6}$ to terminate the simulations. Table 2 gives the thermal properties of material used in the simulations. The laser energy is kept the same for all intensity distributions with different intensity parameters. Figure 2 shows laser intensity distribution for different values of the intensity parameter ($\beta$). Moreover, the power is kept the same as the experimental value in the simulations; in which case the intensity parameter $\beta = 0$, i.e., Gaussian distribution with the parameter $a = 2/3 \times R$ ($R$ is a laser beam radius at the workpiece surface $R = 0.3$ mm) and power intensity $I_o = 0.6 \times 10^{10}$ W/m$^2$.

## Experimental

The laser used in the experiment is a $CO_2$ laser (LC-αIII-Amada; Amada, Cedex, France) and delivering the maximum output power of 2000 W with adjustable duty cycle. Nitrogen emerging from a conical nozzle and co-axially with the laser beam is used. A focal lens of 127 mm is used to focus the laser beam, which results in the focal radius of 0.3 mm at the surface. The laser beam intensity distribution at the workpiece surface was Gaussian. The laser heating parameters are given in Table 3.

## Result and Discussions

Laser repetitive pulse heating of surface of the aluminum coated steel is examined. The alumina coating has 10 $\mu$m thickness at the steel surface. The phase change in alumina and in the surface region of the steel is incorporated in the analysis.

Figure 3 shows temporal variation of temperature at the surface of alumina at alumina-steel interface and at some depth inside steel for 10 laser pulses. It should be noted that each laser pulse has heating and cooling periods due to the duty cycle, which is 60%, i.e., 0.6 × $\tau$ is the heating period

Table 3. Laser Heating Parameters

| Duty Cycle | Power (W) | Nozzle Gap (mm) | Nozzle Diameter (m) | Focus Diameter (m) (mm) | $N_2$ Pressure (kPa) | $a$ (m) |
|---|---|---|---|---|---|---|
| 0.6 | 1500 | 1.5 | $1.5 \times 10^{-3}$ | $0.3 \times 10^{-3}$ | 300 | $0.2 \times 10^{-3}$ |

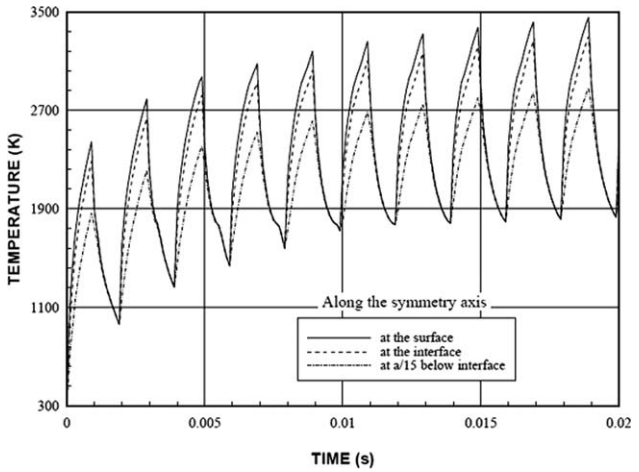


**Figure 3. Temporal variation of temperature at different depths.**

and $0.4 \times \tau$ is the cooling period, $\tau$ being the pulse length. Temperature rises rapidly at the surface and at the other locations below the surface, provided that the rise of temperature is high at the surface. This is attributed to the low thermal conductivity of alumina as compared with steel. In addition, the laser power intensity is the maximum at the surface. The melting temperature of steel is well below the melting temperature of alumina (Table 1); therefore, steel undergoes a melting after the second pulse, whereas alumina remains in the solid phase. Because the phase change in the steel surface takes place rapidly, attainment of constant temperature during the heating cycle is not notable from temperature curve. However, the decay rate of temperature changes in the cooling cycle at the interface and at a depth $a/15$ ($6.7 \times 10^{-5}$ m) below the surface. The change of temperature decay rate in the cooling period of the pulse indicates the presence of the phase change during and after the second pulse. As the time progresses further, temperature increases at the surface and reaches the melting temperature of alumina. In this case, temperature increase changes indicating the initiation of the phase change at the alumina surface. This is more pronounced as the number of the laser pulses increases. Moreover, temperature at interface and at depth $z = 10^{-5}$ m below the interface remains in liquid phase during the 6 and more pulses, because temperature remains above the melting temperature of steel in this region.

Figure 4 shows temperature variation along the radial direction at the surface for the beginnings and endings of 9th and 10th pulses. It should be noted that the laser pulse intensity distribution is Gaussian at the irradiated surface. Consequently, the peak temperature occurs at the irradiated spot center. Temperature reaches its maximum at end of the heating period of the 10th pulse and the difference between the peak temperatures due to 9th and 10th pulses is small. However, temperature difference at the end of the cooling periods of 9th and 10th pulses is negligibly small. Consequently, attainment of the similar distributions of temperature during the heating and cooling cycles prevail that almost steady heating situation is attained after the 9th pulse at the irradiated surface. Temperature decay in the vicinity of the irradiated spot center is lower than that corresponding to next to the surface vicinity. The slow decay of temperature in the irradiated surface is associated with the laser power intensity distribution at the surface. The Gaussian intensity distribution results in the similar temperature distribution at the surface. The phase change, taking place between the solidus and liquidus temperatures, results in almost steady temperature in the radial direction. However, this is not observed at the end of the heating cycle of 9th and 10th pulses. This indicates that the mushy zone, where temperature changes within solidus and liquidus limit, is considerably narrow in the radial direction at the end of the heating period of 9th and 10th pulses. Temperature in the region of the irradiated spot center remains well above the melting temperature of alumina. This shows the super heating in the liquid phase at the alumina surface. However, the region where the superheating takes place is limited to $y = 0.15 \times 10^{-3}$ m from the irradiated spot center. In the case of the end of the cooling period of 9th and 10th pulses, temperature reduces below the melting temperature of alumina. In this case, solid phase heating takes place at the surface. Because the liquid phase occurs in the region of the irradiated spot center, temperature decay along the radial direction in this region is gradual at the end of the cooling period. It should be noted that heat conduction from the superheated liquid to underneath solid surface and heat convection from the surface in radial direction result in almost steady temperature decaying in this region.

Figure 5 shows temperature distribution inside the coating and steel for the periods corresponding to the beginning and ending of 9th and 10th pulses. Temperature decays sharply at the end of the heating cycle of 9th and 10th pulses. In addition, difference in temperature profiles at the end of the heating cycle due to both pulses is significantly small. The mush zones in the alumina coating and in the steel are not observable from temperature curves. This indicates that the size of the mushy zone is significantly narrow in the depth of both alumina coating and steel. In the case of the end of the cooling cycle of 9th and 10th pulses, both temperature profiles become almost similar along the depth. Temperature in the alumina coating remains below the melting temperature; therefore, it remains in the solid phase. However,

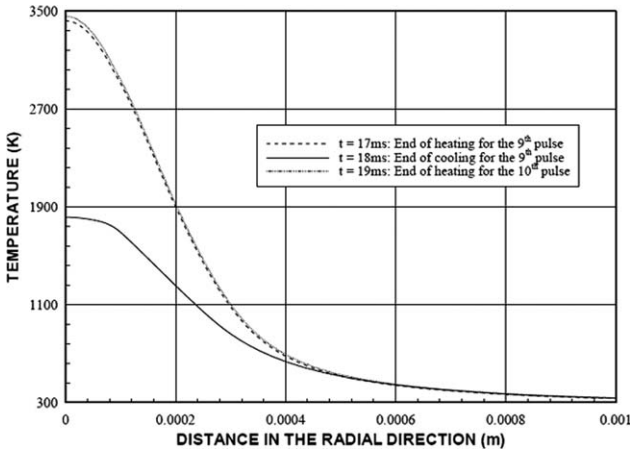


**Figure 4. Temperature distribution along the radial direction for different times.**

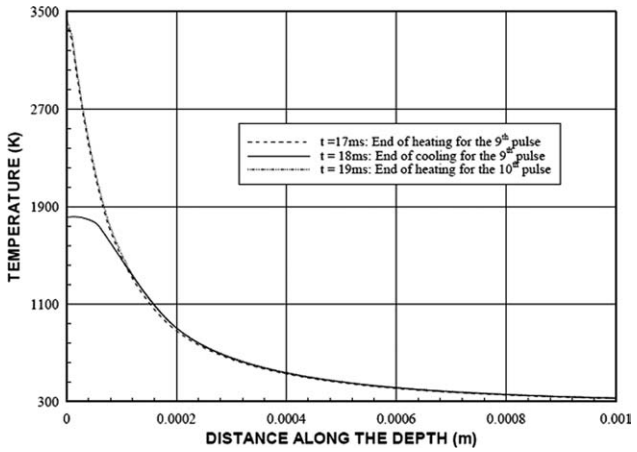


**Figure 5. Temperature distribution inside the substrate material for different times.**

temperature in the steel is above the melting temperature at the interface as well as some depth below the steel surface. This results in almost flat temperature distribution along some depth in steel. Consequently, alumina coating remains in the solid phase, whereas steel surface remains in the liquid phase. As the depth below the steel surface increases temperature decays first gradually and later sharply. The gradual decay of temperature is associated with the superheating of liquid phase in steel. Moreover, the superheating in the liquid phase in steel surface acts as a thermal barrier for heat conduction from the alumina coating. This, in turn, results in the attainment of almost steady temperature in the alumina coating.

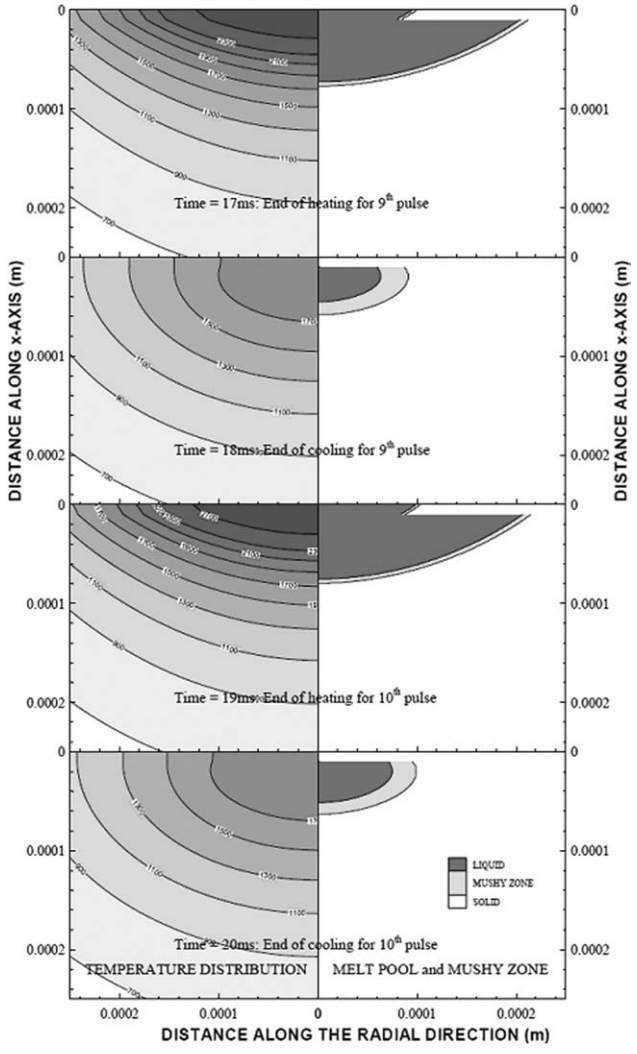


**Figure 6. Temperature contours, liquid and solid phases, and mushy zone.**

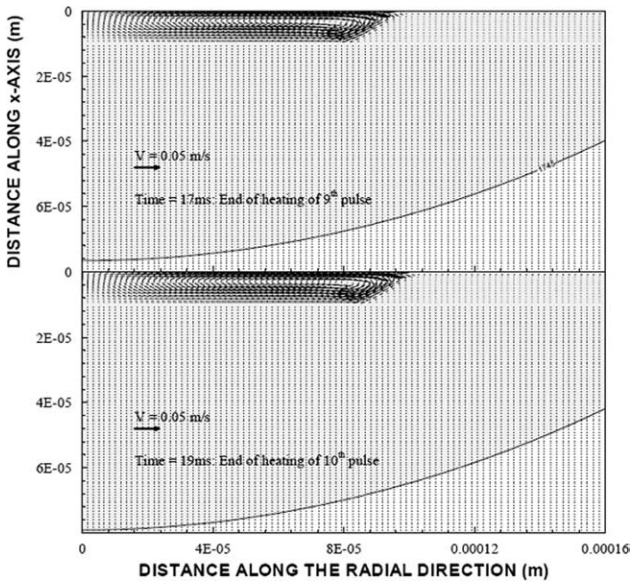


**Figure 7. Velocity vectors in the melt pool for different times.**

Figure 6 shows temperature contours and liquid phase, mushy zone and solid phase at the end of cooling and heating periods of 9th and 10th pulses. The size of the melt pool (width and depth) is larger during the end of the heating period. This remains almost the same for 9th and 10th pulses. In the case of the end of the cooling period, the width of the melt pool reduces more than that corresponding to the melt depth. In addition, alumina coating remains in the solid phase, whereas the melt pool is present in the region of the steel surface beneath the alumina coating. The size of the mushy zone increases at the end of the cooling period of both pulses. This is because of the heat transfer from liquid phase to solid phase at liquid-solid interface. In this case, the high-latent heat of melting of steel is responsible for the increase in the mushy zone size in steel. The melt pool and the mushy zone geometry become round in steel toward the alumina-steel interface. This occurs because of the heat conduction in the radial direction, because the temperature gradient is high in the radial direction in the interfacial region during the cooling period. The size of the melt zone in the radial direction in steel is larger than that corresponding to alumina coating. This is related to the solidus and the liquidus temperatures of alumina and steel; in which case, the solidus and the liquidus temperature are higher for alumina (Table 1). The melt depth predicted agrees with the experimented data as depicted from Figure 7, i.e., the melt depth predicted after 10th pulse is 7.25 $\mu$m while it is 80 $\mu$m corresponding to the experiment. The difference is

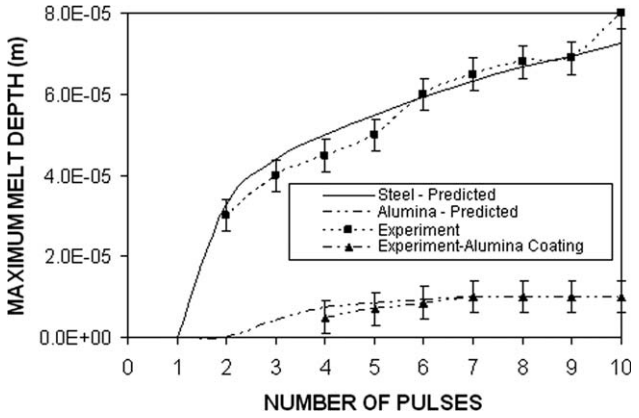


**Figure 8. The maximum depth of melt for each pulse predicted and obtained from the experiment.**

The melt layer of steel is observed while alumina coating was in solid phase in the early pulses.

because of the experimental error, which is in the order of 8% and the assumptions made in the simulations such as uniform properties and assumption of constant surface reflectivity ($r_f = 0.62$). It should be noted that the experimental error is based on the repeatability of the results corresponding three repeats.

Figure 8 shows velocity vectors in the melt pool of alumina due to the Marangoni flow at the end of the heating period of 9th and 10th pulses. However, the velocity vectors in the melt pool of steel are not visible, because the flow in the melt pool is governed by the density variation only, which is not significant. It should be noted that the melt pool in steel does not have a free surface; therefore, the surface tension is omitted in the analysis. Consequently, Marangoni flow replaces with the flow due to density variation in the melt pool of steel. The flow field forms a circulation cell toward the melt pool edge. The maximum velocity magnitude is in the order of 0.4 m/s. The circulation center of the cell is shifted toward the melt pool surface. This is because of: (1) the surface tension gradient ($\frac{\partial \sigma}{\partial T}$), which is high toward the melt pool edge, and (2) the rate of fluid strain, which is high at the melt pool bottom, i.e., resulting in a frictional force, which shifts the cell away from the melt pool wall.

## Conclusions

Laser repetitive pulse heating of alumina-coated steel surface is considered. Temperature field incorporating the phase change in the irradiated region is modeled using the control volume approach. The enthalpy-porosity method is adopted for the phase change. The Marangoni flow in the melt pool is incorporated in the melt pool. The repetitive pulse has a heating and a cooling cycles and the heating cycle is 0.6 of the total pulse, whereas 0.4 of the total pulse corresponds to the cooling cycle. It is found that temperature rise is fast at the alumina-steel interface and in the vicinity of the steel surface during the heating cycle. Steel undergoes the phase change after the second pulse, whereas phase change in alumina occurs at a later heating period. Moreover, temperature rise and decay in the heating and cooling cycles of 9th and 10th pulses became almost the same; in which case, alumina coating and steel surface undergo a phase change during the heating cycle. In the cooling cycle, the solidification occurs in the alumina coating, whereas liquid phase remains in the surface of steel. The solid phase heating is associated with high liquidus and solidus temperatures of alumina. The formation of mushy zone at the liquid–solid interface is not notable in temperature curves, which is due to the small mushy zone size. The melt pool size in steel is higher than that corresponding to alumina. The size of the melt pool in steel surface changes during the cooling period of 9th and 10th pulses. In this case, the melt pool becomes rounded towards the alumina-steel interface. This indicates the high rate of thermal conduction taking place in between the mushy zone and the solid phase along the radial direction. A circulation cell is formed in alumina due to the Marangoni effect. However, the flow ceases in the melt pool of steel, because steel does not have a free surface and the density variation is small in steel melt pool.

## Acknowledgments

The authors acknowledge the support of King Fahd University of Petroleum and Minerals, Dhahran, Saudi Arabia.

## Notation

$a$ = Gaussian parameter ($m$)
$A_{mush}$ = mushy zone constant
$c_p$ = specific heat capacity, J/(kg k)
$E$ = total energy per unit mass, J/kg
$H$ = total enthalpy, J
$h$ = enthalpy, J/kg
$h_{ref}$ = reference enthalpy, J/kg
$h_t$ = heat-transfer coefficient, W/(m$^2$ K)
$I_o$ = laser peak power intensity, W/m$^2$
$k$ = thermal conductivity, W/m K
$L$ = latent heat of melting, J/kg
$r$ = radial distance, m
$r_f$ = reflection coefficient
$S$ = momentum sink per unit mass flow rate, m/s
$S_o$ = source term, W/m$^3$
$T$ = temperature, K
$T_{liquidus}$ = liquid temperature, K
$T_{solidus}$ = solid temperature, K
$T_o$ = initial temperature, °C
$t$ = time, s
$\bar{v}$ = velocity vector, m/s
$\bar{v}_{liq}$ = liquid velocity in the mushy zone, m/s
$z$ = axial distance, m

### *Greek letters*

$\alpha(=\frac{k}{\rho C_{p_s}})$ = thermal diffusivity, m$^2$/s
$\beta_l$ = the liquid fraction
$\beta_E$ = volumetric thermal expansion coefficient, K$^{-1}$
$\Delta$ = absorption depth ($6.17 \times 10^7$), m$^{-1}$
$\varepsilon$ = porosity
$\rho$ = density, kg/m$^3$

## Literature Cited

1. Zhang Y, Faghri A. Vaporization, melting and heat conduction in the laser drilling process. *Int J Heat Mass Transfer*. 1999;42:1775–1790.
2. Yang LX, Peng XP, Wang BX. Numerical modeling and exerimental investigation on the characteristics of molten pool during laser processing. *Int J Heat Mass Transfer*. 2001;44:4465–4473.
3. Chakraborty S, Dutta P. Numerical modeling of heat and mass transfer in laser surface alloying: non-equilibrium solidification effects. *Mater Manuf Process*. 2002;17:455–468.

4. Tani G, Tomesani L, Campana G. Prediction of melt geometry in laser cutting. *Appl Surf Sci*. 2003;208–209:142–147.
5. Chung H, Das S. Numerical modeling of scanning laser-induced melting, vaporization and resolidification in metals subjected to step heat flux input. *Int J Heat Mass Transfer*. 2004;47:4153–4164.
6. Li JF, Li L, Stott FH. Comparison of volumetric and surface heating surfaces in the modeling of laser melting of ceramic materials. *Int J Heat Mass Transfer*. 2004;47:1159–1174.
7. Quintero F, Pou J, Fernandez JL, Doval AF, Lusquinos F, Boutinguiza M, Soto R, Perez-Amor M. Optimization of an off-axis nozzle for assist gas injection in laser fusion cutting. *Opt Lasers Eng*. 2006;44:1158–1171.
8. Safdar S, Li L, Sheikh MA, Liu Z. An analysis of the effect of laser beam geometry on laser transformation hardening. *J Manuf Sci Eng*. 2006;128:659–667.
9. Konrad C, Zhang Y, Shi Y. Melting and resolidification of a subcooled metal powder particle subjected to nanosecond laser heating. *Int J Heat Mass Transfer*. 2007;50:2236–2245.
10. Krishnan S, Murthy JY, Garimella SV. Analysis of solid-liquid phase change under pulsed heating. *J Heat Transfer*. 2007;129: 395–399.
11. Yilbas BS, Naqavi IZ, Shuja SZ. Modeling and experimental study into the laser: assisted nitriding of Ti-6Al-4V. *ASME J Manuf Sci Eng*. 2002;124:863–874.
12. Yilbas BS, Naqavi IZ. Laser heating including phase change process and thermal stress generation in relation to drilling. *Proc Inst Mech Eng Part B: J Eng Manuf*. 2003;217:977–991.
13. Yilbas BS, Mansoor SB. Laser pulse heating and phase changes in the irradiated region: temperature dependent thermal properties case. *Int J Thermal Sci*. 2009;48:761–772.
14. Bin-Mansoor S, Yilbas BS. Laser pulse heating of steel surface: consideration of phase change process. *Numer Heat Transfer Part A: Appl*. 2006;50:787–807.
15. Bin-Mansoor S, Yilbas BS, Shuja SZ. Laser pulse heating: modeling of cavity formation. *Proc Inst Mech Eng Part C: J Mech Eng Sci*. 2007;221:307–328.
16. Shuja SZ, Yilbas BS, Khan S. Laser consecutive pulse heating in relation to melting influence of duty on melting. *Heat Mass Transfer*. 2009;45:793–803.
17. Shuja SZ, Yilbas BS, Khan S. Laser consecutive pulse heating and phase change: influence of spatial distribution of laser pulse intensity on melting. *Int J Thermal Sci*. 2009;48:1960–1966.
18. Fluent, Inc. *Fluent Users Guide*. New York: Fluent, Inc., 2005.
19. Voller VR, Prakash C. A fixed-grid numerical modeling methodology for convection-diffusion mushy region phase-change problems. *Int J Heat Mass Transfer*. 1987;30:1709–1720.
20. Shuja SZ, Yilbas BS. Pulsative heating of surfaces. *Int J Heat Mass Transfer*. 1998;41:3899–3918.
21. Patankar SV. *Numerical Heat Transfer*. New York: McGraw-Hill, 1980.
22. Incropera FP, DeWitt DP. *Fundamentals of Heat and Mass Transfer*, 4th ed. New York: Wiley, 1996:829–830.

*Manuscript received Aug. 4, 2010.*